Topological Feature Tracking for Submesoscale Eddies

Sam Voisin[1], Jay Hineman[1], James B. Polly[1], Gary Koplik[1], Ken Ball[1], Paul Bendich[1,4], Joseph D'Addezio[2], Gregg A. Jacobs[2], Tamay Özgökmen[3]

[1]Geometric Data Analytics, Inc., Durham, NC, USA
[2]Ocean Dynamics and Prediction, Naval Research Laboratory, Stennis Space Center, MS, USA
[3]Rosenstiel School of Marine and Atmospheric Science, University of Miami, FL, USA
[4]Department of Mathematics, Duke University, Durham, NC, USA

Key Points:

- Current procedures for studying submesoscale oceanographic features assume independence between features identified at different times.
- Statistics from these methods oversample features and cannot determine the lifetime evolution of the transient submesoscale processes.
- We apply the Topological Feature Tracking algorithm to identify and track eddies over time, which yields unique, time-varying statistics.

Corresponding author: James B. Polly, `james.polly@geomdata.com`

Abstract

Current state-of-the art procedures for studying modeled submesoscale oceanographic features have made a strong assumption of independence between features identified at different times. Therefore, all submesoscale eddies identified in a time series were studied in aggregate. Statistics from these methods are illuminating but oversample identified features and cannot determine the lifetime evolution of the transient submesoscale processes. To this end, the authors apply the Topological Feature Tracking (TFT) algorithm to the problem of identifying and tracking submesoscale eddies over time. TFT allows a user to identify submesoscale eddies as critical points on a set of time-ordered scalar fields and associate the points between consecutive timesteps. The procedure yields tracklets which represent spatio-temporal displacement of eddies. Thus the time-dependent behavior of submesoscale eddies can be studied. We analyze the submesoscale eddy dataset produced by TFT, which yields unique, time-varying statistics on this currently underexplored phenomenon.

Plain Language Summary

Current state-of-the art procedures for studying small-scale features in the ocean do not take the effects of time into account. Instead, features like small vortices are studied as a single population across many points in time. This method has provided oceanographers with many valuable insights. New insights can be added by identifying vortices and then tracking them over time to study their behavior through an algorithm designed to identify and track features on a grid.

1 Introduction

Submesoscale eddies are important ocean features which occupy length scales between large-scale forcings and micro-scale dissipation. Their larger, mesoscale counterparts are well studied, yet submesoscale currents have, until recently, received less attention despite the important role played in a variety of oceanic transport phenomena. In addition to influencing the transport of nutrients (Lévy et al., 2018) and pollutants (Poje et al., 2014), submesoscale currents form an important link in the turbulent energy cascade and the global oceanic circulation (see McWilliams, 2016, for a summary of submesoscale eddy dynamical theory, observational findings, and modeling approaches).

Studies considering the temporal evolution of mesoscale eddies have been performed (e.g., Chelton et al., 2007; Kurian et al., 2011; Faghmous et al., 2015), but similar investigations have yet to be done for the submesoscale. Statistical summaries of submesoscale eddy properties, behavior, and lifetime evolution are of interest to multiple communities as the nature of these disturbances inform both modeling approaches to simulate eddy dynamics, and satellite altimetry data assimilation.

While dissipation-scale phenomena are typically unresolved and parameterized with subgrid-scale closure models, the "intermediate" length scales occupied by submesoscale eddies are being resolved in models such as the Navy Coastal Ocean Model (NCOM; Barron et al., 2006) and the Regional Oceanic Modeling System (ROMS; Shchepetkin & McWilliams, 2005). Time tracking and statistical reporting of submesoscale eddies in these models is not currently done but would provide additional insight on eddy lifetime, directionality, and behavior. This information is useful for model evaluation, e.g., inspecting performance of eddy viscosity and parameterized closure schemes. Furthermore, statistical summaries of transient submesoscale eddy behavior is needed for data assimilation efforts (D'Addezio et al., 2019) and has motivated the statistical investigations in D'Addezio et al. (2020).

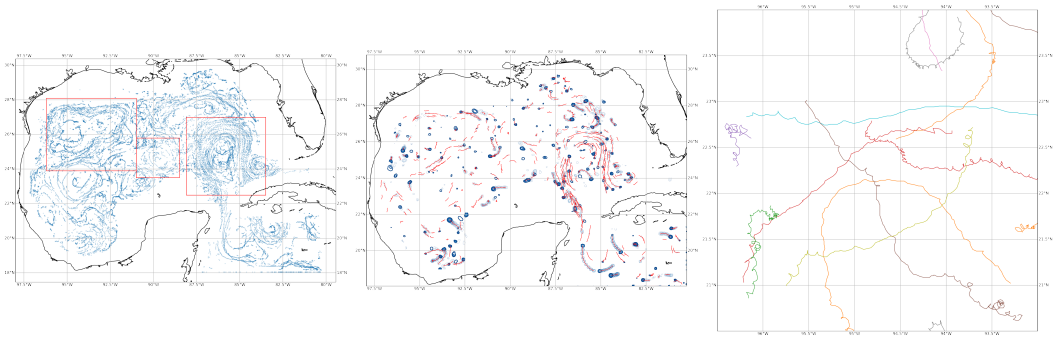

Figure 1: Left to right: (1) Submesoscale eddies identified in space and time depicted as blue points in the Gulf of Mexico. Zones 1, 2 and 3 (west to east) enclose mesoscale features which transport eddies. Eddy characteristics in these zones are explored in the following sections. (2) Submesoscale eddies being tracked through time via TFT. Solid line contours are eddies identified at January 5, 2016 03:00. Dotted line contours depict eddy locations over the previous five days. This subset depicts only tracks of 25km or longer. (3) Selection of tracks of eddies lasting for 15 days or more. These relatively long lived tracks demonstrate both the cyclic behavior and transport behavior of the eddies.

In this study we apply the algorithm (henceforth referred to as Topological Feature Tracking, or TFT) introduced in Soler et al. (2018) to the problem of submesoscale eddy identification and temporal association. In this way, we extend the study of D'Addezio et al. (2020) by computing statistics of eddy lifetimes and trajectories to supplement the time-independent statistical analysis presented therein. Using one year of NCOM simulation data, we provide statistical summaries of eddy speed, lifespan, and displacement in aggregate over the Gulf of Mexico. We also provide analysis of these characteristics conditioned on season and regions selected for the presence of mesoscale features. While extending the technique used in D'Addezio et al. (2020) with the TFT-based method, we are introducing the community to the TFT approach in the context of surface-based submesoscale eddies.

2 Method

In this section we give a brief description of the TFT algorithm (Section 2.2), along with the elementary topological data analysis (TDA) concepts needed to understand it (Section 2.1). For more details on TFT and TDA in general, see Soler et al. (2018) and Edelsbrunner and Harer (2010), respectively. Finally, we describe the Okubo–Weiss parameter used to generate the scalar field to which we apply TFT (Section 2.3).

2.1 Persistence Diagrams

Suppose that f is a *scalar field*, that is, a real-valued function on some domain U. The domain can be of arbitrary dimension and shape and we do not need to make any assumptions about the smoothness of f. For a working example, suppose U is any of the two-dimensional squares shown on the left side of Figure 2, with the values of f indicated by the color bar. The *persistence diagrams* of f provide a compact summary of the location and importance of topological features as observed by f. More precisely, consider $U_\alpha = \{x \in U \mid f(x) \leq \alpha\}$. As the threshold value α increases, these create a nested *filtration* of *sublevel sets* that start with the empty set and finish with U itself. Along the way, topological features such as *connected components* and *holes* are created and

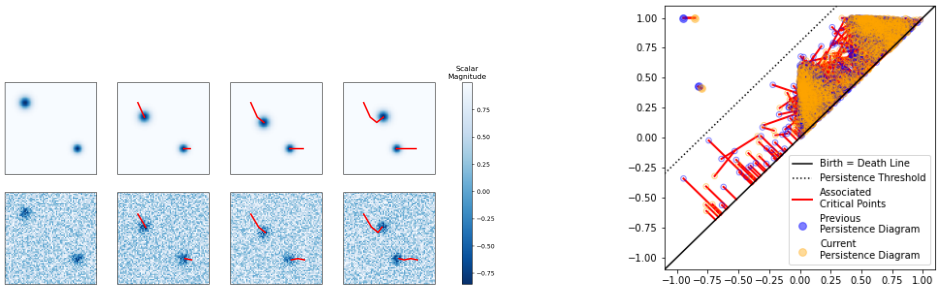

Figure 2: Illustration of TFT algorithm on a notional example: Left: Tracking two Gaussian features on a time-ordered series of scalar fields. Right: Matching between persistence diagrams (blue dots and orange dots) associated to scalar fields at $t = 2, 3$, respectively.

then subsequently destroyed, each of which corresponds (Milnor, 1963) to a *critical point* of f that occurs at a *critical value*. The birth and death critical values of each feature are plotted as dots in the plane, and the multi-set of such dots, along with the major diagonal $y = x$, forms the persistence diagram $D(f)$ of the scalar field. Two such diagrams can be seen on the right side of Figure 2, where blue (orange) dots correspond to features in the scalar fields in the second (third) columns, bottom row. The *persistence* of a dot is the difference between its death and birth values (i.e, the vertical distance to the major diagonal). Higher-persistence dots tend to be less likely to be noise. For example, all of the example scalar fields have two prominent connected components indicated by the two dots far from the major diagonal.

Persistence diagrams have two important properties that we exploit in this paper. First, they are *stable to noise* in a precise sense. The *Wasserstein distance* between two diagrams can be defined as the cost of an optimal matching between the dots in the diagrams, where dots can be matched to the major diagonal if needed; the right side of Figure 2 shows an optimal matching. Precise theorems (Cohen-Steiner et al., 2007) bound the Wasserstein distance between two diagrams $D(f), D(g)$ in terms of the ℓ_∞ distance between the scalar fields f, g. In particular, this guarantees that the diagrams associated to a smoothly time-varying sequence of scalar fields will themselves form a time-varying sequence, which facilitates the TFT algorithm. Second, various theorems (Edelsbrunner et al., 2006; Laudenbach, 2013) guarantee the following: given a two-dimensional scalar field f and a threshold value ϵ, there exists a simplified scalar field g with exactly the same critical point structure of f except that all critical points of persistence less than ϵ have been removed. For example, with ϵ being the distance between the major diagonal and the dotted line on the right side of Figure 2, the scalar fields in the top row on the left are the topological simplifications of the scalar fields in the bottom row.

2.2 Topological Feature Tracking

Now suppose that we have a time-ordered sequence $f_1, \ldots f_T$ of scalar fields, such as the four fields across either row on the left of Figure 2, all defined on the same domain U. Computing persistence leads to a time-ordered sequence $D(f_1), \ldots, D(f_T)$ of persistence diagrams. The user has the option of choosing a persistence threshold to topologically simplify the scalar fields as desired. Then the TFT algorithm connects certain critical points to produce a series of *tracks*, as follows.

Consider a time-adjacent pair of (possibly simplified) scalar fields f_i and f_{i+1}. Each dot in the two diagrams corresponds to a topological feature, and has associated to it a pair of critical points in U, one which created the feature and one which destroyed it. The *lifted Wasserstein* distance of Soler et al. (2018) defines the cost of associating two dots in $D(f_i)$ and $D(f_{i+1})$ as a (user-specified) weighted combination of the distance between the pair of dots in the persistence diagram and the geometric distance between the associated critical points in the domain U, and an optimal matching between the two diagrams is then computed via this cost function. If this optimal matching connects two dots, then a track segment is drawn between their associated critical points. If it connects a dot at time i with the diagonal at time $t+1$, then a track segment ends. If it connects a dot at time $i+1$ with the diagonal at time i, a new track segment is started. The end result, over all time steps in the sequence, is a set of tracks which move in time through the domain U.

Figure 2 shows the outputted tracks for our notional example, indicated as thick red lines on the left side of the figure. Figure 1 shows tracks for submesoscale eddies, identified by the same procedure and further described in the following sections.

The matching procedure described above must be applied to each consecutive pair of persistence diagrams in the time series. Computationally, this may be done in parallel so long as the time order is maintained. Once matching is completed for all consecutive time steps, the matchings of associated critical pairs may be applied to coordinates in the domain to combine the track segments and form full tracks of the identified features.

2.3 Okubo–Weiss Parameter

The above describes the TFT method applied to a time-ordered series of arbitrary scalar fields. Our application is concerned with a specific scalar field, called the *Okubo–Weiss* parameter.

Following D'Addezio et al. (2020), this is defined as

$$W = S_n^2 + S_s^2 - \zeta^2 \tag{1}$$

S_n and S_s are the normal and shear components of the strain respectively while ζ represents relative vorticity. A location at which $|\zeta| > S_n^2 + S_s^2$ implies $W < 0$ thus a high relative vorticity at that location. Regions having this quality may be interpreted as eddies.

3 Data & Procedure

The dataset used in this paper is a year-long simulation of the Gulf of Mexico generated by the Navy Coastal Ocean Model (NCOM). The dataset has a spatial resolution of one kilometer. The data were provided with temporal resolution of three hours. The time period of this dataset ranges from January 1, 2016 at 00:00 to December 31, 2016 at 21:00. Two derivative datasets were generated from the NCOM simulation. The first is an exact replication of the dataset generated in D'Addezio et al. (2020). We call this the "masked" dataset—where all Okubo–Weiss values outside of the submesoscale eddy region are masked, and only eddies remain (see D'Addezio et al., 2020 for details). The second dataset is a less stringent version of the first in which the same procedure is followed until the normalized Okubo–Weiss field W_N is generated. We refrain from applying the second smoothing filter and circularity test from this dataset; we therefore refer to it as "unmasked" as the entire Okubo–Weiss field remains, thus tasking the TFT algorithm to perform eddy identification.

We apply the TFT algorithm to the negative portions of each scalar field in both datasets. The negative portions of the scalar fields represent vortices. We found that limiting the field to only negative values resulted in the best track quality.

The output of the TFT algorithm is a set of tracks representing the historical behavior of individual submesoscale eddies in the Gulf of Mexico. Two mild postprocessing routines were applied to this set of tracks. We first removed tracks which began or ended on the boundary of the Gulf of Mexico. These erroneous tracks are caused by the abrupt end of the scalar field at its edges. We also applied a filter which removed any tracks whose average speed was greater than the maximum surface speed at any point in the NCOM simulation. A subset of the resulting tracks can be seen in the middle and right images of Figure 1.

4 Results

In this section we provide insights gleaned from tracking submesoscale eddies identified in the Okubo–Weiss field. In Section 4.1 we share figures which depict large scale features' influence on submesoscale eddy transport. In Section 4.2 we provide descriptive statistics of submesoscale eddy behavior observed through tracks identified using TFT.

4.1 Identifying Seasonal Mesoscale Patterns via Submesoscale Tracks

Mesoscale features are responsible for transporting submesoscale eddies throughout the Gulf of Mexico. By tracking those submesoscale eddies as they are transported, we are able to gain insight into the evolving behavior of the mesoscale phenomena as well. Figure 3 depicts this behavior in large scale features through their influence on submesoscale eddies. Each frame of Figure 3 represents three months of tracks of submesoscale eddies $\geq$ 25 km in length. Beginning in the top left image (winter), the greatest submesoscale eddy track density appears in the Loop Current passing north between Cuba and the Yucatán Peninsula and exiting the Gulf between the tip of Florida and northern coast of Cuba. We are able to watch the continued deformation of this Loop Current throughout the year by observing its shifting impact on the trajectories of local submesoscale eddies. By the spring (bottom left image) the Loop Current has split into a lower current exiting the gulf to the east and a mesoscale eddy off the western coast of Florida. By the summer (top right) this large eddy has moved west, and a greater density of tracks appear in the east bound current. Finally in the fall the large mesoscale eddy appears to have largely dissipated while the current continues to carry a high density of eddies to the east. Across all seasons, the submesoscale tracks do not follow any consistent directional pattern. Their flow appears predominantly determined by the large-scale background flow, that being dictated primarily by both the synoptic jet and the interior mesoscale eddies. This is in contrast with the mesoscale eddy field which is known to propagate westward outside the influence of boundary currents (Chelton et al., 2007).

4.2 Statistical Summary of Tracks

We provide descriptive statistics of tracks generated by features identified on the Okubo–Weiss fields in Table 1. We calculate track statistics in aggregate within the Gulf of Mexico for an entire year as well as on subsets of the tracks. We subset tracks temporally by season (winter, spring, summer and fall) as well as spatially in three "zones" associated with large scale features. These zones are depicted in the left image of Figure 1. These zones are labeled Zone 1, Zone 2 and Zone 3 from west to east. Zone 1 is an irregularly shaped, counterclockwise flow. Zone 2 is a circular, counterclockwise pattern. Zone 3 is a clockwise flow passing north between Cuba and the Yucatán Peninsula, reaching its zenith and turning south before passing between the Florida Keys and Cuba's northern coast.

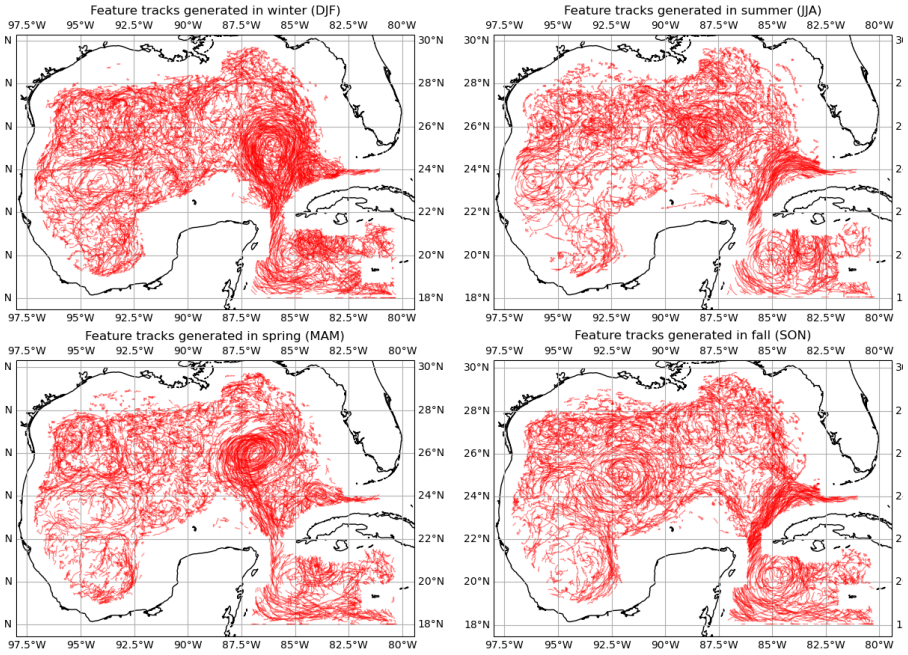

Figure 3: Illustration of submesoscale eddy behavior in aggregate over four seasons of the NCOM dataset. We can see changes in the large scale features responsible for transporting submesoscale eddies here. Tracks have been filtered down to those greater than or equal to 25km for these images.

Broadly, eddies in the Gulf of Mexico tend to move fastest in the spring and summer. However, the seasonal variance is low. Overall, submesoscale eddy velocity is $O(0.5$ m/s), furthering previous results which showed mesoscale and submesoscale horizontal velocities to be similar (Capet et al., 2008). If, as we have documented, the submesoscale eddy motion is largely a function of the jet and mesoscale eddies (Figure 1), this horizontal velocity proportionality is consistent

Lifespans tend to be longer in the winter and fall. This is likely due to the known relationship between submesoscale generation and maintenance, and the depth of the mixed layer (McWilliams, 2016). Using this relationship, one can calculate a mixed-layer deformation radius that dictates the maximum size of submesoscale eddies as a function of mixed-layer depth. In the summer, the mixed layer shoals in the presence of strong surface heating, dramatically reducing the mixed-layer deformation radius. With a 1-km horizontal resolution, this NCOM simulation cannot support the generation and maintenance of such small features, leading to a decline in the number of identified submesoscale eddies during this season (D'Addezio et al., 2020). As is found here, any submesoscale eddy generated by the model during this time period is likely to be short lived because mixed layer dynamics are not favorable. This is further supported by the seasonality of the submesoscale eddy sample size (Table 1; last column). In contrast, winter features much deeper mixed layers, and can therefore support the creation of more, relatively larger submesoscale eddies and allow them to propagate longer in the more favorable mixed layer environment.

Finally, displacements tend to be similar across seasons for the unmasked group while eddies identified in the masked dataset tend to travel further during the winter and fall months. Note that both distances and lifetimes are greater for the unmasked fields, compared with the masked fields. This is due to the limiting nature of traditional eddy identification methods (e.g., D'Addezio et al., 2020). Certain criteria for identification, e.g., "circularity" may change over the eddy lifetime such that the feature fails to meet the identification criteria at some instances. This is an advantage of using TFT for this purpose so as to capture a more complete lifespan of an eddy rather than omit features in the middle of their evolution due to lacking circularity or other identification criteria.

	Speed (m/s)		**Lifespan (h)**		**Displacement (km)**		**Sample Size**	
	Unmasked	**Masked**	**Unmasked**	**Masked**	**Unmasked**	**Masked**	**Unmasked**	**Masked**
	Mean (St. Dev.)	**Mean (St. Dev.)**	**Mean (St. Dev.)**	**Mean (St. Dev.)**	**Mean (St. Dev.)**	**Mean (St. Dev.)**		
GoM Aggregate	**0.4436 (0.2343)**	**0.3808 (0.2124)**	**17.8 (28.8)**	**12.3 (26.0)**	**30.9 (60.4)**	**16.2 (31.4)**	**655,727**	**119,775**
GoM Winter (DJF)	0.4184 (0.2333)	0.3760 (0.2171)	19.0 (30.5)	13.5 (27.6)	31.3 (62.0)	17.4 (33.7)	182,522	31,319
GoM Spring (MAM)	0.4726 (0.2367)	0.3949 (0.2167)	16.7 (25.7)	11.1 (20.7)	31.4 (58.5)	15.4 (27.3)	171,134	31,292
GoM Summer (JJA)	0.4703 (0.2354)	0.3928 (0.2156)	15.8 (25.1)	11.6 (27.6)	29.1 (54.9)	15.8 (32.8)	154,453	28,545
GoM Fall (SON)	0.4133 (0.2241)	0.3586 (0.1966)	19.4 (33.3)	13.0 (27.5)	31.6 (66.0)	16.1 (31.7)	147,618	28,619
Zone 1 Aggregate	**0.4316 (0.2154)**	**0.3457 (0.1689)**	**18.4 (30.0)**	**12.8 (26.4)**	**30.9 (58.9)**	**15.2 (28.6)**	**141,626**	**27,081**
Zone 1 Winter	0.3862 (0.2034)	0.3205 (0.1598)	20.6 (33.7)	14.6 (29.3)	31.1 (61.2)	16.1 (30.1)	38,219	6,859
Zone 1 Spring	0.4556 (0.2189)	0.3526 (0.1697)	17.8 (26.8)	11.3 (20.2)	32.0 (58.2)	13.8 (22.9)	39,754	7,848
Zone 1 Summer	0.4622 (0.2187)	0.3596 (0.171)	16.3 (25.7)	11.6 (26.5)	29.5 (53.7)	14.4 (29.1)	35,998	6,737
Zone 1 Fall	0.4200 (0.2106)	0.3501 (0.1727)	19.1 (33.4)	14.2 (29.8)	30.8 (63.0)	17.2 (32.8)	27,655	5,637
Zone 2 Aggregate	**0.4315 (0.2172)**	**0.3725 (0.1887)**	**16.8 (29.0)**	**12.8 (27.1)**	**26.6 (47.8)**	**16 (30.9)**	**24,571**	**5,773**
Zone 2 Winter	0.4137 (0.2101)	0.3528 (0.1745)	18.2 (29.8)	13.8 (26.7)	27.5 (47.4)	16.1 (27.3)	6,601	1,506
Zone 2 Spring	0.4304 (0.2187)	0.3523 (0.1837)	15.6 (25.9)	12.2 (20.9)	25.2 (44.6)	14.4 (22.4)	5,576	1,443
Zone 2 Summer	0.4887 (0.2317)	0.4427 (0.2218)	13.6 (21.6)	11.3 (28.8)	25.2 (46.5)	17.0 (35.2)	5,481	1,245
Zone 2 Fall	0.4040 (0.2019)	0.3542 (0.1631)	18.8 (34.9)	13.6 (30.7)	27.8 (51.6)	16.6 (36.5)	6,913	1,579
Zone 3 Aggregate	**0.5167 (0.2513)**	**0.4917 (0.2566)**	**14.8 (24.3)**	**12.0 (22.3)**	**29.3 (52.9)**	**21.0 (38.0)**	**93,578**	**19,608**
Zone 3 Winter	0.5196 (0.2581)	0.5177 (0.2642)	16.4 (25.6)	12.5 (23.6)	33.1 (59.6)	23.1 (42.2)	29,903	5,849
Zone 3 Spring	0.5621 (0.2464)	0.5459 (0.2562)	13.8 (21.2)	10.9 (17.2)	30.5 (54.0)	21.9 (37.6)	23,629	4,813
Zone 3 Summer	0.5275 (0.2458)	0.4833 (0.2536)	13.5 (21.5)	11.3 (22.2)	27.1 (47.8)	19.3 (35.5)	22,881	4,773
Zone 3 Fall	0.4348 (0.2333)	0.4023 (0.2238)	15.3 (28.8)	13.2 (25.4)	23.7 (43.8)	18.8 (34.5)	17,165	4,173

Table 1: A selection of descriptive statistics of submesoscale eddy tracks across the Gulf of Mexico and in each of the three zones depicted in Figure 1. Statistics for the Gulf of Mexico and each zone are calculated in aggregate as well as by season.

5 Conclusions

Our application of TFT to submesoscale eddy tracking provides new insights into the behavior of small scale structures in the ocean. Through studying the movement patterns of submesoscale eddies, we improve our understanding of the mesoscale phenomena that are responsible for their transport. Neither labeled training data nor long training epochs were required for tracking eddies in the Gulf of Mexico. TFT may be similarly applied to any section of the ocean and indeed to any evolving scalar field.

Future work may focus on tracking meso- and submesoscale eddies entangled within the same field. Further modifying the Lifted Wasserstein distance function to penalize incorrect matchings in a nonlinear manner will improve the method broadly. Additionally, an automated method of suggesting or selecting weight parameters and the persistence threshold may be explored.

Open Research

Data Availability Statement: Ocean surface velocity data, used to identify and track features in this study, were obtained via the Navy Coastal Ocean Model (NCOM). The solution data used herein was generated using the same NCOM modeling framework (i.e., domain, boundary and initial conditions, numerical and physical parameterizations, etc.) as described in D'Addezio et al. (2020) (`https://doi.org/10.1175/JPO-D-19-0100.1`).

Acknowledgments
Research by the first six authors was partially supported by the DARPA Ocean of Things project, under contract N6600121C4006. Joseph M. D'Addezio was funded by the Office of Naval Research (ONR) under grant N0001421WX02086. Gregg Jacobs and Tamay Özgökmen were funded by the DARPA Ocean of Things project under contract HR0011150953. This document has been cleared for public release under Distribution Statement "A" (Approved for Public Release, Distribution Unlimited). The views, opinions and/or findings expressed are those of the authors and should not be interpreted as representing the official views or policies of the Department of Defense or the U.S. Government.

References

Barron, C. N., Kara, A. B., Martin, P. J., Rhodes, R. C., & Smedstad, L. F. (2006). Formulation, implementation and examination of vertical coordinate choices in the global navy coastal ocean model (ncom). *Ocean Modelling*, *11*(3-4), 347–375.

Capet, X., McWilliams, J., Molemaker, M., & Shchepetkin, A. (2008). Mesoscale to submesoscale transition in the california current system part i: Flow structure, eddy flux, and observational tests. *J. Phys. Oceanogr.*, *38*, 29-43.

Chelton, D. B., Schlax, M. G., Samelson, R. M., & de Szoeke, R. A. (2007). Global observations of large oceanic eddies. *Geophysical Research Letters*, *34*(15).

Cohen-Steiner, D., Edelsbrunner, H., & Harer, J. (2007, January). Stability of persistence diagrams. *Discrete Comput. Geom.*, *37*(1), 103–120. Retrieved from `http://dx.doi.org/10.1007/s00454-006-1276-5` doi: 10.1007/s00454-006-1276-5

D'Addezio, J. M., Jacobs, G. A., Yaremchuk, M., & Souopgui, I. (2020). Submesoscale eddy vertical covariances and dynamical constraints from high-resolution numerical simulations. *Journal of Physical Oceanography*, *50*(4), 1087–1115.

D'Addezio, J. M., Smith, S., Jacobs, G. A., Helber, R. W., Rowley, C., Souopgui, I., & Carrier, M. J. (2019). Quantifying wavelengths constrained by simulated swot observations in a submesoscale resolving ocean analysis/forecasting

system. *Ocean Modelling*, *135*, 40–55.

Edelsbrunner, H., & Harer, J. (2010). *Computational topology: an introduction*. AMS.

Edelsbrunner, H., Morozov, D., & Pascucci, V. (2006). Persistence-sensitive simplification functions on 2-manifolds. In *Proceedings of the twenty-second annual symposium on computational geometry* (pp. 127–134).

Faghmous, J. H., Frenger, I., Yao, Y., Warmka, R., Lindell, A., & Kumar, V. (2015). A daily global mesoscale ocean eddy dataset from satellite altimetry. *Scientific data*, *2*(1), 1–16.

Kurian, J., Colas, F., Capet, X., McWilliams, J. C., & Chelton, D. B. (2011). Eddy properties in the california current system. *Journal of Geophysical Research: Oceans*, *116*(C8).

Laudenbach, F. (2013). A proof of morse's theorem about the cancellation of critical points. *Comptes Rendus de l'Academie des Sciences*, 483–488.

Lévy, M., Franks, P. J. S., & Smith, K. S. (2018). The role of submesoscale currents in structuring marine ecosystems. *Nature communications*, *9*(1), 1–16.

McWilliams, J. C. (2016). Submesoscale currents in the ocean. *Proceedings of the Royal Society A: Mathematical, Physical and Engineering Sciences*, *472*(2189), 20160117.

Milnor, J. W. (1963). *Morse theory*. Princeton University Press.

Poje, A. C., Özgökmen, T. M., Lipphardt, B. L., Haus, B. K., Ryan, E. H., Haza, A. C., ... others (2014). Submesoscale dispersion in the vicinity of the deepwater horizon spill. *Proceedings of the National Academy of Sciences*, *111*(35), 12693–12698.

Shchepetkin, A. F., & McWilliams, J. C. (2005). The regional oceanic modeling system (roms): a split-explicit, free-surface, topography-following-coordinate oceanic model. *Ocean modelling*, *9*(4), 347–404.

Soler, M., Plainchault, M., Conche, B., & Tierny, J. (2018). Lifted wasserstein matcher for fast and robust topology tracking. *2018 IEEE 8th Symposium on Large Data Analysis and Visualization (LDAV)*, 23–33. doi: 10.1109/ldav.2018.8739196

Figure 1.

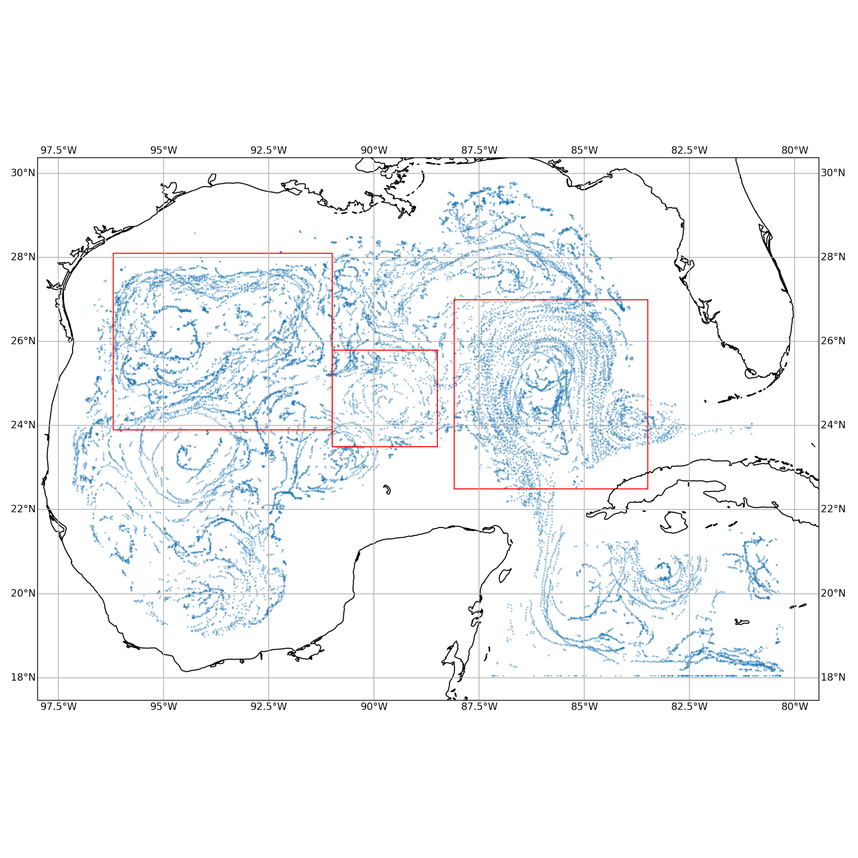
97.5°W
95°W
92.5°W
90°W
87.5°W
85°W
82.5°W
80°W
30°N
28°N
26°N
24°N
22°N
20°N
18°N

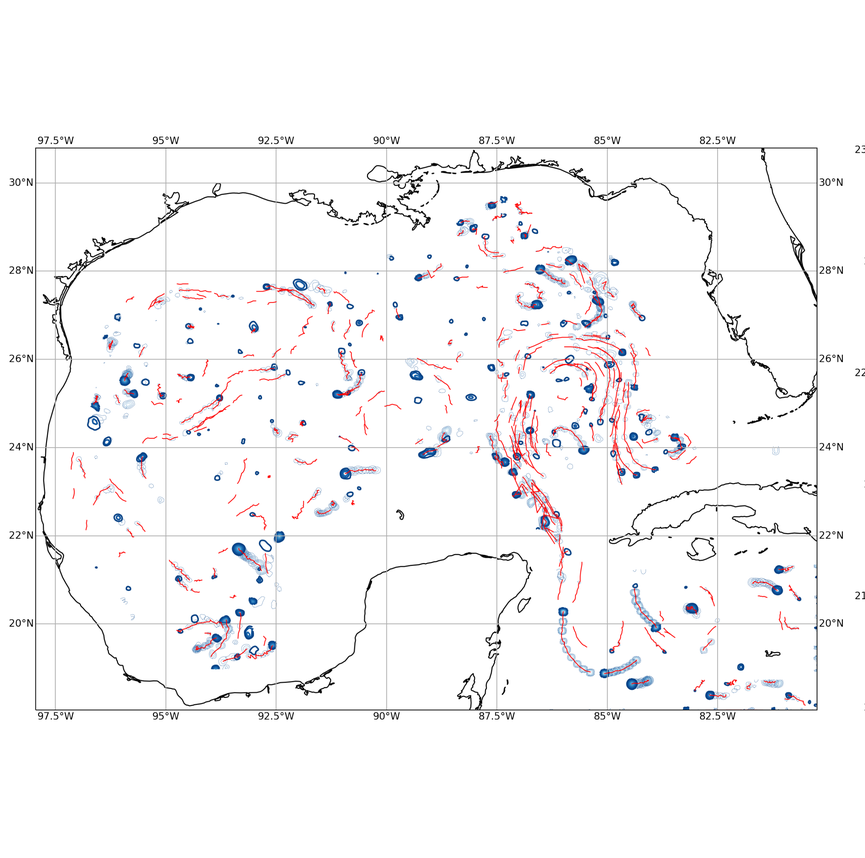
97.5°W
95°W
92.5°W
90°W
87.5°W
85°W
82.5°W
30°N
28°N
26°N
24°N
22°N
20°N

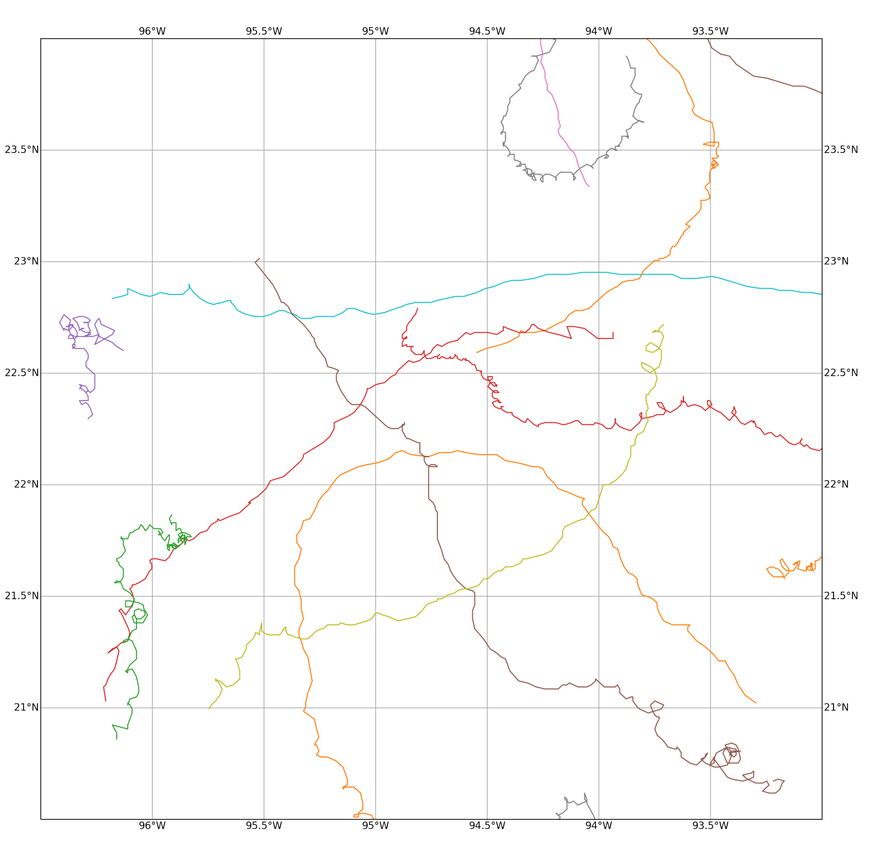
96°W
95.5°W
95°W
94.5°W
94°W
93.5°W
23.5°N
23°N
22.5°N
22°N
21.5°N
21°N

Figure 2, RHS.

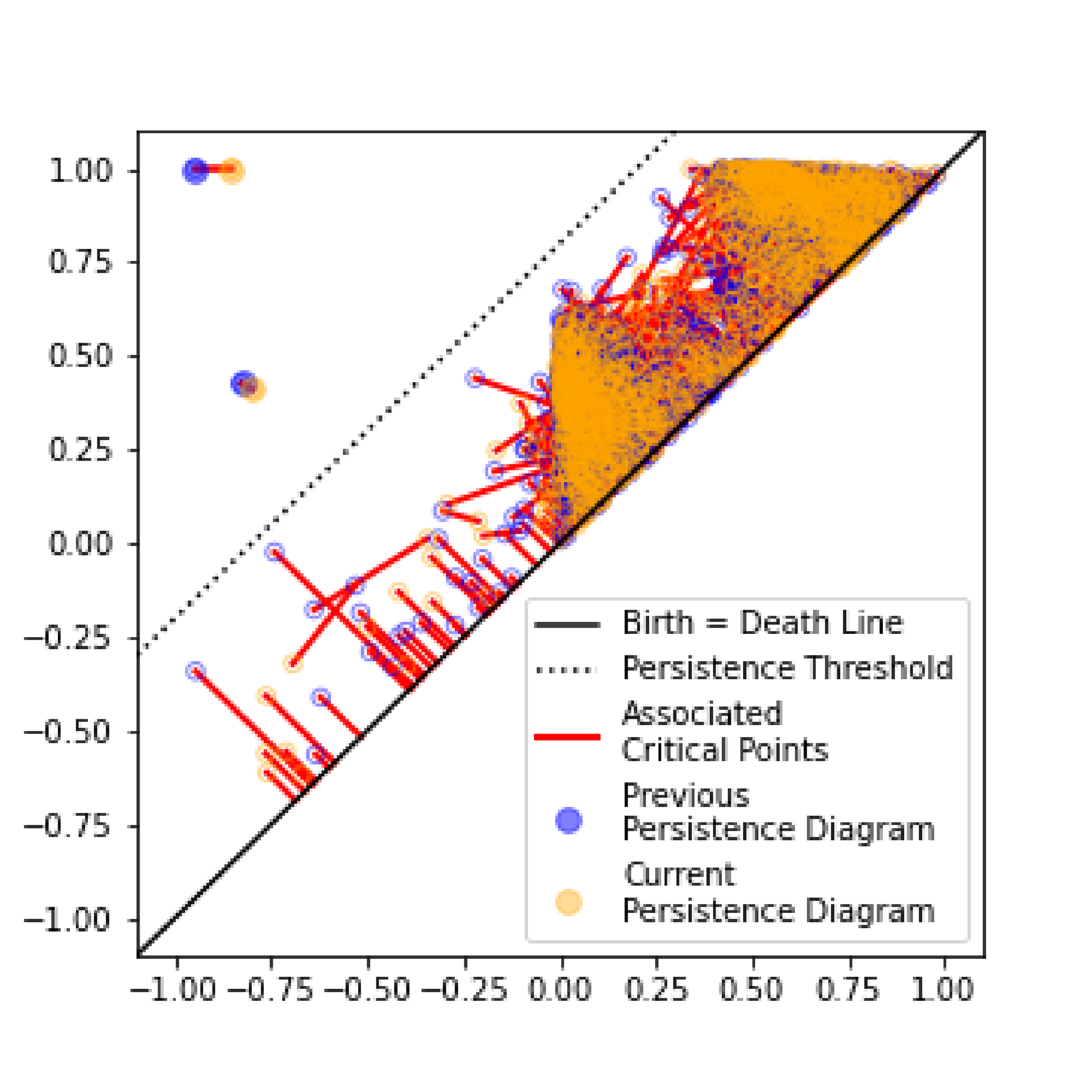
1.00
0.75
0.50
0.25
0.00
−0.25
−0.50
−0.75
−1.00
−1.00 −0.75 −0.50 −0.25 0.00 0.25 0.50 0.75 1.00
Birth = Death Line
Persistence Threshold
Associated
Critical Points
Previous
Persistence Diagram
Current
Persistence Diagram

Figure 3.

Feature tracks generated in winter (DJF)

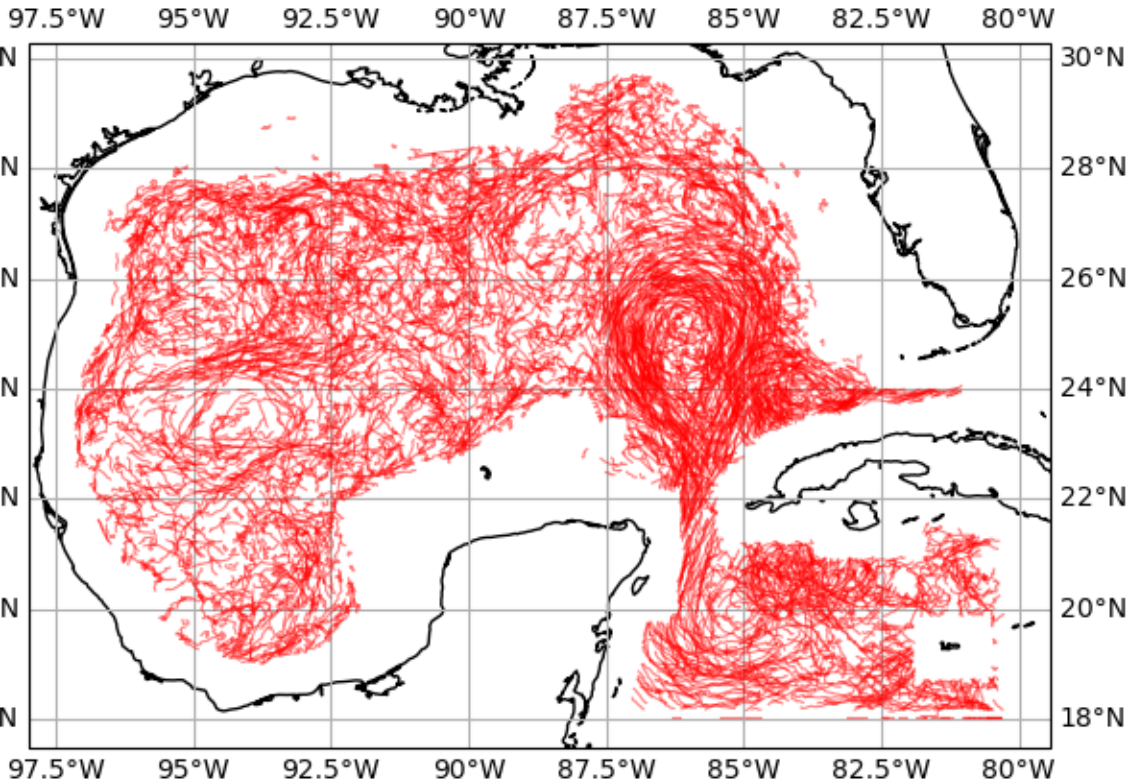

Feature tracks generated in summer (JJA)

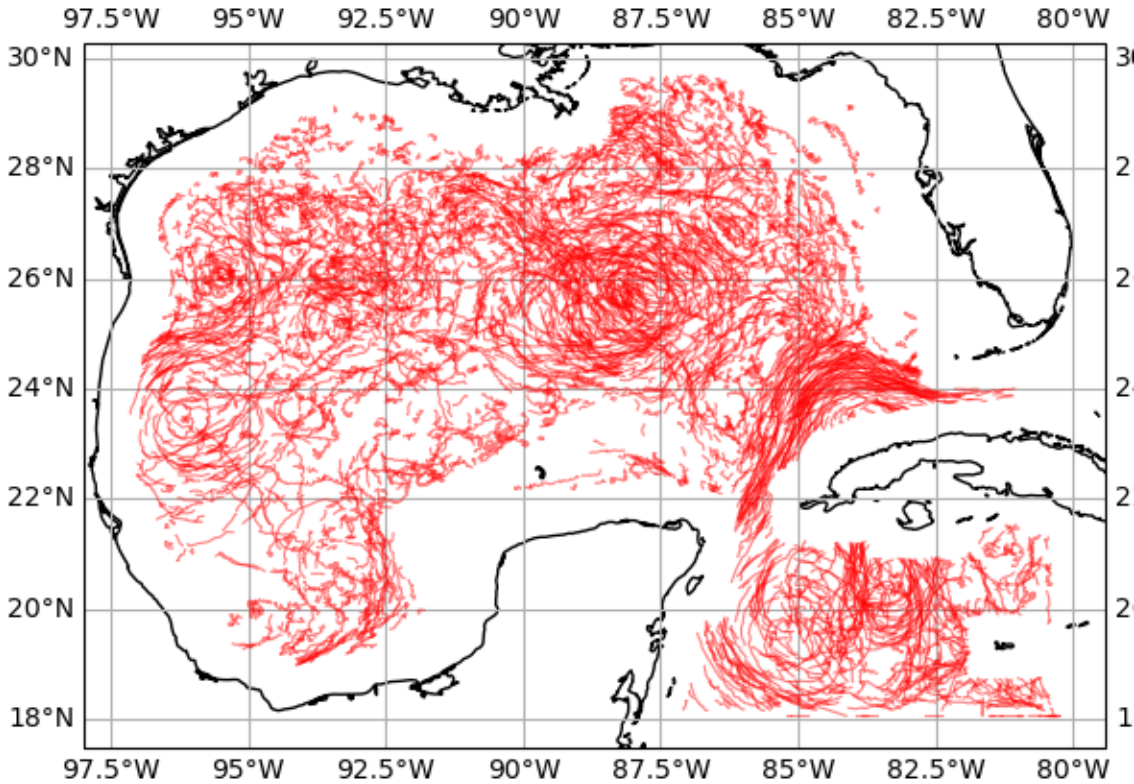

Feature tracks generated in spring (MAM)

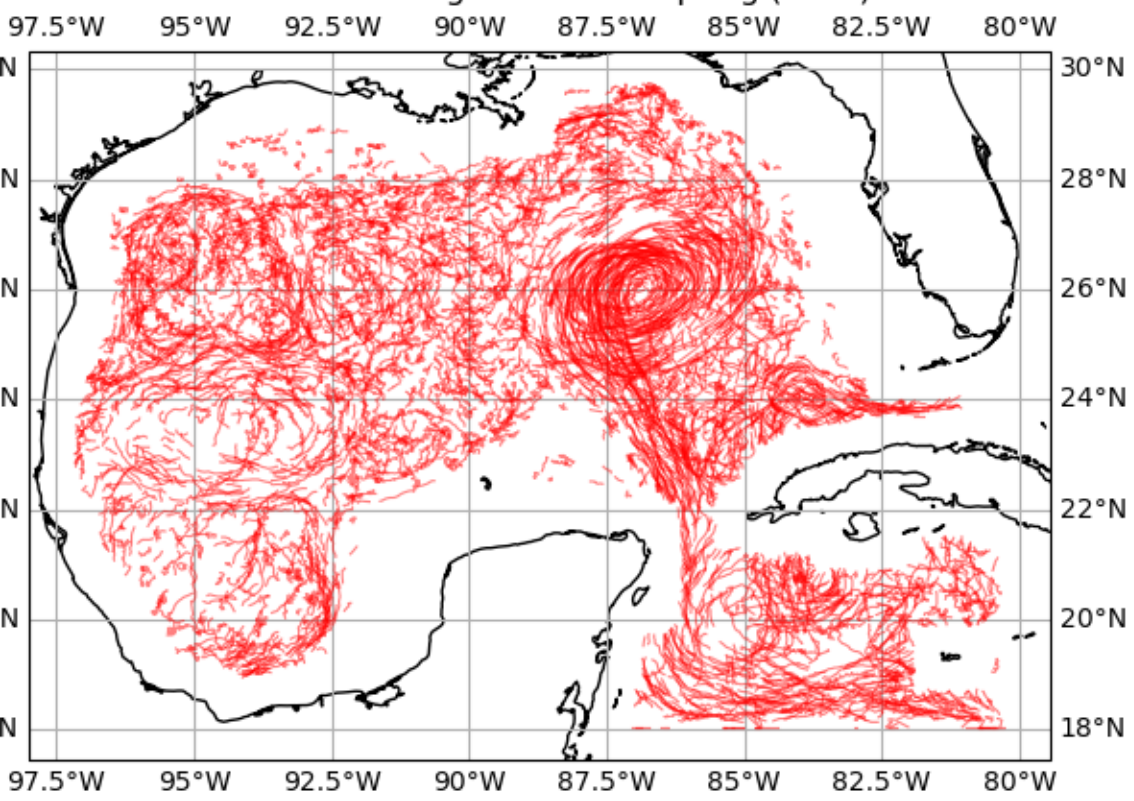

Feature tracks generated in fall (SON)

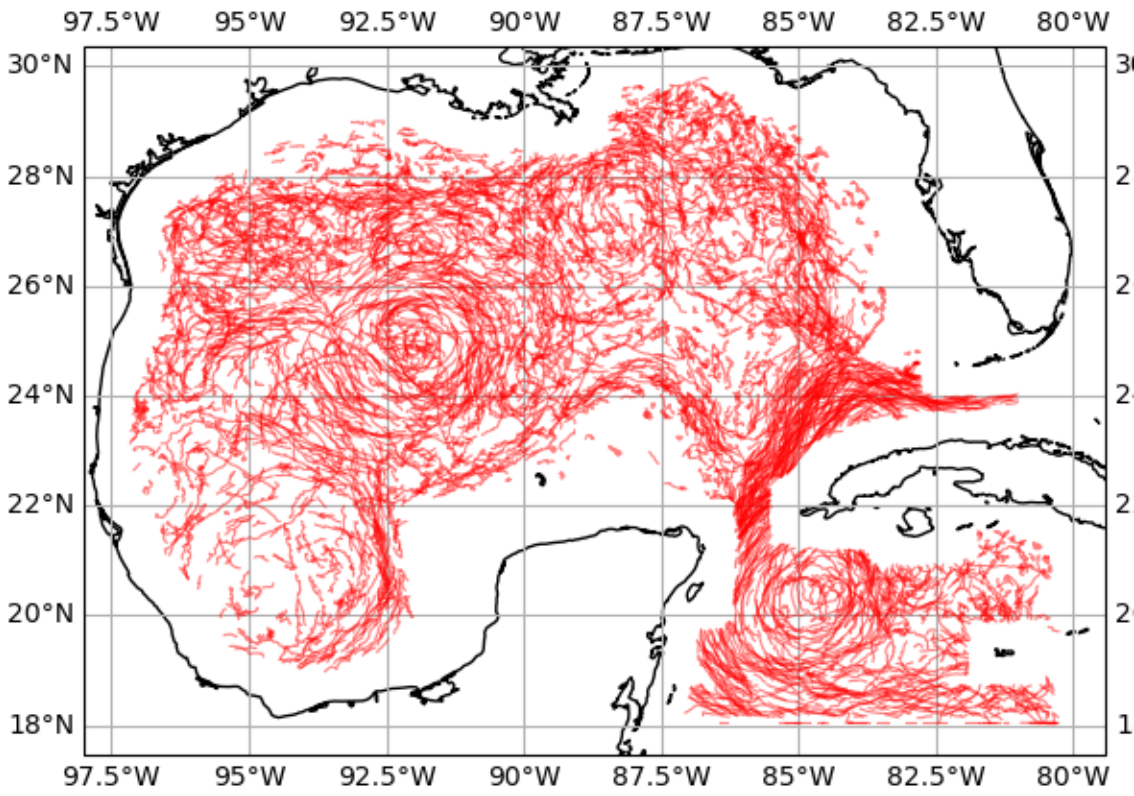

Figure 2, LHS.

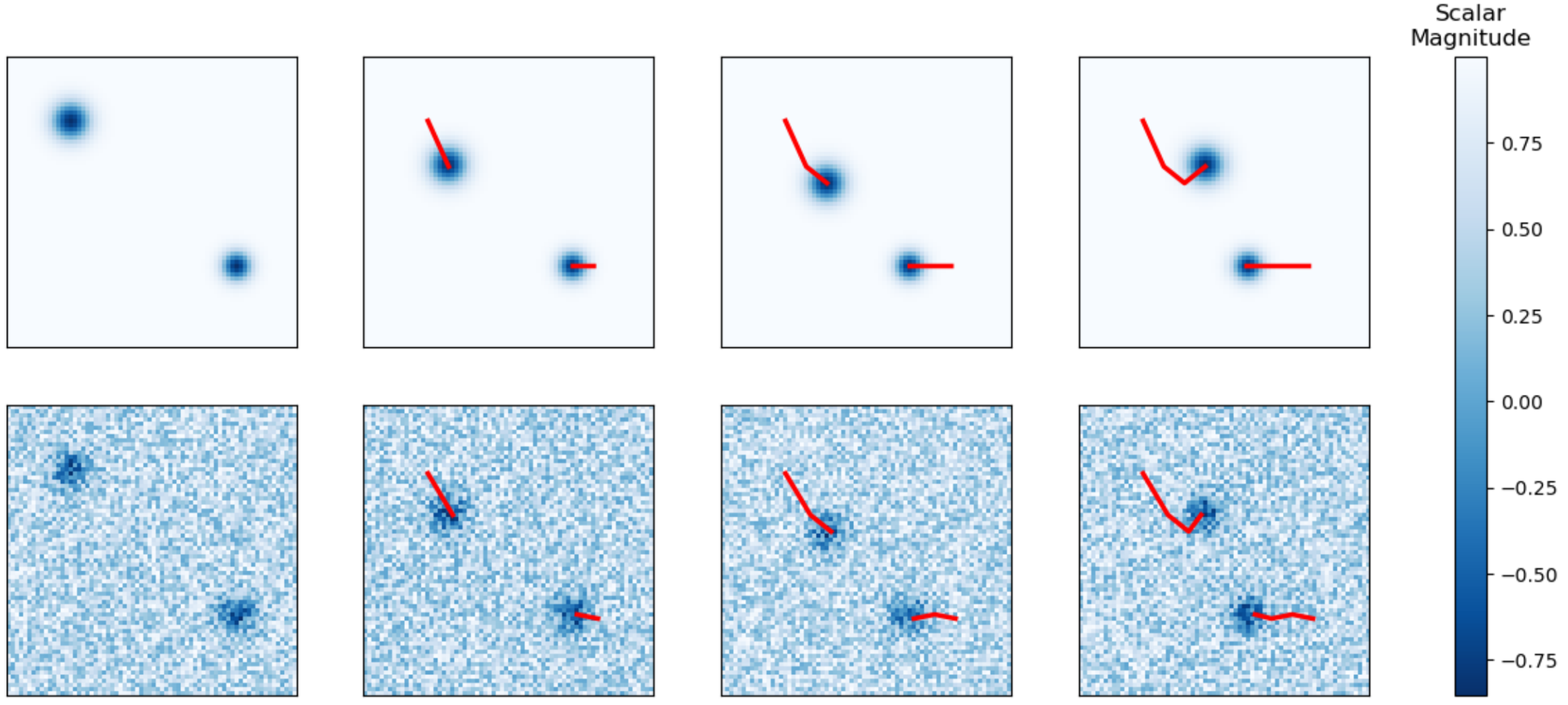
Scalar
Magnitude
0.75
0.50
0.25
0.00
−0.25
−0.50
−0.75